Electromagnetics

Electromagnetic Induction Imaging of Metallic Objects at Multiple Depths

Maryam Ravan^{1*}, Reza K. Amineh^{1*}, Anwar Hussein^{1,2}, Oleksiy Simanov¹, and Ashutosh Agarwal¹

- ¹ Department of Electrical and Computer Engineering, New York Institute of Technology, New York, NY 10023, USA
- ² Department of Electrical and Computer Engineering, Rowan University, Glassboro, NJ 08028, USA
- * Senior Member, IEEE

Abstract—In this letter, a novel approach is presented for imaging of metallic objects based on induction sensing. The approach relies on the concept of collection of the point-spread function (PSF) in a linear space-invariant system. For this purpose, the responses of small objects are measured a priori to serve as the PSFs of the imaging system. Then, these PSFs are employed in a test scenario, in which, the response of unknown objects distributed over multiple depths are measured and inverted to reconstruct two-dimensional (2D) images at those depths. The stack of these 2D images provides a 3D image. The image reconstruction is fast due to the use of forward and inverse Fourier transforms. This imaging approach is validated via the use of off-the-shelf components.

Index Terms—Electromagnetics, Eddy Currents, Imaging and Sensing, Inductive Sensing.

I. INTRODUCTION

Imaging of metallic objects has a wide range of applications in infrastructure imaging (e.g., see [Szymanik 2016]), non-destructive testing (e.g., see [Darrer 2015]), security screening (e.g., see [Ledger 2015]), biomedical imaging (e.g., see [Gogola 2013]), etc. In a common imaging technique, called electromagnetic induction imaging (EII) [Peyton 1996], electromagnetic waves with sufficiently low frequency, are employed to illuminate the medium under inspection. The use of low frequencies allows for penetration inside the medium and producing eddy currents on the surface of hidden metallic objects. These eddy currents, in turn, produce secondary electromagnetic fields that reflect back toward the transmitter. These secondary electromagnetic fields carry information about the type, size, and shape of the hidden metallic objects.

The EII has been exploited for biomedical imaging [Peyton 1996, Griffiths 2001, Zolgharni 2010], non-destructive testing [Higson 2003, Gaydecki 2002, Wei 2012], and national nuclear security [Darrer 2015]. In [Ma 2013], a planar array system, including an array of 4 × 4 coils, has been proposed for three-dimensional (3D) subsurface imaging. There, a linear inverse solver along with Tikhonov regularization have been utilized to calculate the conductivity distribution in the inspected domain. Besides, retrieving depth information has been achieved by using non-adjacent coils.

Recently, high-sensitivity detection and imaging have been implemented based on EII systems. For instance, in [Gaydecki 2002], Q-detection sensors have been used for condition monitoring of steel reinforcing bars embedded in concrete. Besides, an inductance-capacitance resonance system has been proposed for detection of metallic wear debris in rotating and reciprocating machinery [Du 2012, Du 2013]. In [Guilizzoni 2015], a measurement system has been reported based on a resonant LCR circuit which has shown promising results for 2D imaging of metallic samples. This method

has been extended in [Guilizzoni 2016], demonstrating imaging of conductive samples shielded by conductive barriers.

Along the above-mentioned efforts, here, we propose a fast and cost-effective approach to perform imaging of metallic objects at multiple depths. The imaging system is assumed to be linear and space-invariant so that we can employ the convolution theory [Oppenheim 1999]. The inversion approach is fast due to the use of forward and inverse Fourier transforms (FTs). The performance of the approach is validated via the use of off-the-shelf components.

II. THEORY

Fig. 1 illustrates the proposed imaging setup including a transmitter coil illuminating the metallic objects with electromagnetic waves while moving over a rectangular aperture. Multiple receiver coils move together with the transmitter coil to scan the back-scattered field over the aperture. To increase the sensitivity of measuring secondary fields, a capacitor can be connected in parallel with each coil to build an LC tank circuit resonating at frequency f_0 as:

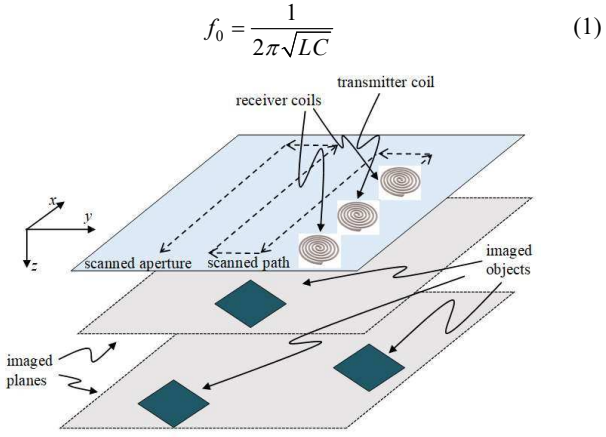


Fig. 1. Illustration of the EII technique which employs a transmitter coil and multiple receiver coils scanning a 2D aperture.

Page 2 of 5 IEEE MAGNETICS LETTERS

Then, the presence of metallic objects can be detected via measuring the change in the resonant frequency. Here, to be able to image objects at multiple depths, we propose data acquisition with N_r receiver coils. Assume that at each sampling position (x, y), the resonant frequencies are measured for all the receiver coils. The objective is then to reconstruct images over $z = z_i$ planes where $i = 1, ..., N_z$. In the following, we refer to the measured resonant frequencies as just responses.

In the proposed imaging technique, we assume that the imaging system is linear and space-invariant (LSI). The linear property is based on the assumption that multiple reflections between the metallic objects are ignored and the objects are small. On the other hand, space-invariant property indicates that if the objects are shifted in a plane parallel to *x-y* plane in Fig. 1, their responses will be shifted by the same amount and along the same direction. Assuming that the imaging system is LSI allows for the use of convolution theory.

According to the convolution theory for an LSI system, the response to any arbitrary input function to the system can be written in terms of the convolution of the point-spread function (PSF) of the system and that input function. PSF of the system is actually the response of the system to a Dirac delta function.

Here, in order to collect the PSFs, we record the responses R^{co} due to small objects placed at $(0, 0, z_i)$, $i = 1, ..., N_z$. We refer to these small objects as calibration objects (COs). These are the smallest objects that can be measured at $(0, 0, z_i)$ positions. Responses measured for such small objects approximate the responses of the imaging system to Dirac delta input functions. These COs are placed, one at a time, at each $(0, 0, z_i)$, $i=1,...,N_z$ position and their responses $R_i^{co}(x,y)$ are measured over the aperture by scanning the transmitter and receiver coils. Then, the response $R_i(x,y)$ due to any object under tests (OUT) at plane $z = z_i$, can be obtained by the convolution of the collected PSF for the corresponding plane with the OUT's spatial distribution function $c_i(x,y)$. This is written as:

$$R_{i}(x, y) = R_{i}^{co}(x, y) *_{x} *_{y} c_{i}(x, y)$$
 (1)

where $*_x$ and $*_y$ denote convolutions with respect to the x and y variables, respectively. Equation (1) can be written for responses created by the OUTs over each imaged plane $(0, 0, z_i)$, $i = 1, ..., N_z$. Then, the total response R(x, y) measured by the receiver coil due to the presence of the OUTs at all imaged planes can be approximated with the superposition of the contribution of all these responses as:

$$R(x,y) = \sum_{i=1}^{N_z} R_i(x,y) = \sum_{i=1}^{N_z} R_i^{\text{co}}(x,y) *_x *_y c_i(x,y)$$
(2)

In the above equation, $R_i^{co}(x,y)$ functions are known due to the measurement of the responses for COs. R(x,y) is also known due to the recording of the response for the OUTs. In order to estimate the unknown functions $c_i(x,y)$ on the imaged planes $z = z_i$, $i = 1,..., N_z$, the responses are acquired with N_r receiver coils with various sizes allowing for various inspection depths. Thus, (2) can be re-written for the measured responses of each coil. This provides the following system of equations:

$$R(x,y,1) = \sum_{i=1}^{N_z} R_i^{co}(x,y,1) *_x *_y c_i(x,y)$$

$$\vdots$$

$$R(x,y,N_r) = \sum_{i=1}^{N_z} R_i^{co}(x,y,N_r) *_x *_y c_i(x,y)$$
(3)

In order to solve the system of equations in (3), 2D FTs with respect to x and y variables are applied on both sides of the equations. This leads to the following system of equations in the Fourier domain:

$$\begin{cases} \tilde{\tilde{R}}(k_x, k_y, 1) = \sum_{i=1}^{N_z} \tilde{\tilde{R}}_i^{\text{co}}(k_x, k_y, 1) \tilde{\tilde{c}}_i(k_x, k_y) \\ \vdots \\ \tilde{\tilde{R}}(k_x, k_y, N_r) = \sum_{i=1}^{N_z} \tilde{\tilde{R}}_i^{\text{co}}(k_x, k_y, N_r) \tilde{\tilde{c}}_i(k_x, k_y) \end{cases}$$

$$(4)$$

where $\tilde{R}(k_x,k_y,r)$, $\tilde{R}_i^{\rm co}(k_x,k_y,r)$ and $\tilde{c}_i(k_x,k_y)$ are the 2D FTs of the functions R(x,y,r), $R_i^{\rm co}(x,y,r)$, and $c_i(x,y)$, respectively, and k_x and k_y are Fourier variables corresponding to the x and y variables, respectively.

Here, we apply beamspace methodology to each system of equations in (4) (written at each spatial frequency pair (k_x,k_y)). Beamspace processing contains passing the FT of the measured data vector $\mathbf{b} = [\tilde{R}(k_x,k_y,1),...,\tilde{R}(k_x,k_y,N_r)]$ through a linear transformation that reduces sensitivity to correlation between the objects in adjacent imaged surfaces [Rodriguez-Rivera 2006]. In fact, each \mathbf{b} is multiplied by a matrix that reduces the dimension of \mathbf{b} before solving the system of equations. Dimension reduction is obtained by designing the beamspace transformation to focus on a specific imaged surface. The term beamspace was chosen because the spatial response of the dimension-reducing measured data were designed to form a set of overlapping directional beams that has large gain on a specific imaged surface and low gain elsewhere.

We first re-write (4) at each (k_x, k_y) in a matrix form as:

$$\mathbf{b}(k_x, k_y) = \mathbf{A}(k_x, k_y) \mathbf{x}(k_x, k_y) , \qquad (5)$$

where

$$\mathbf{b}(k_{x},k_{y}) = \begin{bmatrix} \tilde{R}(k_{x},k_{y},1) \\ \tilde{R}(k_{x},k_{y},2) \\ \vdots \\ \tilde{R}(k_{x},k_{y},N_{r}) \end{bmatrix},$$
(6)

$$\mathbf{A}(k_{x},k_{y}) = \begin{bmatrix} \tilde{R}_{1}^{\text{co}}(k_{x},k_{y},1) & \cdots & \tilde{R}_{N_{z}}^{\text{co}}(k_{x},k_{y},1) \\ \vdots & \ddots & \vdots \\ \tilde{R}_{1}^{\text{co}}(k_{x},k_{y},N_{r}) & \cdots & \tilde{R}_{N_{z}}^{\text{co}}(k_{x},k_{y},N_{r}) \end{bmatrix}, \quad (7)$$

$$\mathbf{x}(k_{x},k_{y}) = \begin{bmatrix} \tilde{c}_{1}(k_{x},k_{y}) \\ \tilde{c}_{2}(k_{x},k_{y}) \\ \vdots \\ \tilde{c}_{N_{z}}(k_{x},k_{y}) \end{bmatrix} . \tag{8}$$

We then propose an approach for beamspace transformation that is optimized to preserve objects within each imaged surface. We indicate the beamspace transformation using the $N_r \times 1$ matrix **T** and obtain the $M < N_r$ dimensional beamspace data vectors as $\mathbf{b}_{\mathrm{T}}(k_x,k_y) = \mathbf{T}'\mathbf{b}(k_x,k_y)$. We assume that the columns of **T** are orthonormal without loss of generality. The design of matrix **T** is based on minimizing the average error between the original and beamspace representation of the object images. The beamspace data is interpreted as the data in the space spanned by the columns of **T**. Therefore, the component that is not considered in beamspace is the projection of the data onto the space orthogonal to **T**, i.e., $(\mathbf{I} - \mathbf{T}'\mathbf{T})\mathbf{b}(k_x,k_y)$. This implies that the squared error associated with

IEEE MAGNETICS LETTERS Page 3 of 5

mapping an object at a specific imaged plane z_i , $i = 1, ..., N_z$ into beamspace is

$$e_{\mathbf{T}}^{2}(i) = \left\| (\mathbf{I} - \mathbf{T}\mathbf{T}')\mathbf{A}_{i} \right\|_{2}^{2}, \tag{9}$$

where A_i is the i^{th} column of matrix A. In general, an appropriate selection of T will lead to a small error in all imaged surfaces. One method for choosing matrix T could be based on minimizing the mean squared representation error (MSRE) between the original and beamspace representation of the objects in each specific surface

$$\min_{\mathbf{T}} \left(e_{\mathbf{T}}^2(i) \right) \tag{10}$$

Using (9), the minimization problem (10) is equivalent to the maximization problem:

$$\max \operatorname{tr}(\mathbf{T}'\mathbf{G}\mathbf{T})$$
 subject to $\mathbf{T}'\mathbf{T} = \mathbf{I}$ (11)

where

$$G = A_i A_i, i = 1, 2, ... N_z$$
. (12)

The solution to (11) is obtained by choosing the columns of **T** as the eigenvectors corresponding to the M largest eigenvalues of **G**. Therefore, the corresponding minimum MSRE is given by the sum of the $N_r - M$ smallest eigenvalues of **G**. Here, since \mathbf{A}_i is an $N_r \times 1$ vector, the rank of matrix **G** is one and therefore M = 1. Then, the matrix **T** is obtained by choosing the eigenvector corresponding to the largest eigenvalue.

Beamspace algorithm operates on the beamspace-frequency data vector at each (k_x,k_y) , i.e. $\mathbf{b}_{\mathrm{T}}(k_x,k_y)$. Therefore, the matrix $\mathbf{A}(k_x,k_y)$ must be mapped into beamspace to obtain:

$$\mathbf{A}_{\mathrm{T}}(k_{\mathrm{r}}, k_{\mathrm{v}}) = \mathbf{T}' \mathbf{A}(k_{\mathrm{r}}, k_{\mathrm{v}}). \tag{13}$$

Then, the following system of equations:

$$\mathbf{b}_{\mathrm{T}}(k_{\mathrm{r}}, k_{\mathrm{v}}) = \mathbf{A}_{\mathrm{T}}(k_{\mathrm{r}}, k_{\mathrm{v}}) \mathbf{x}(k_{\mathrm{r}}, k_{\mathrm{v}}) \tag{14}$$

is solved in the beamspace at each (k_x,k_y) to obtain the values for $\tilde{c}_i(k_x,k_y)$ at the corresponding imaged planes $z_i,\ i=1,...,\ N_z$. The algorithm is repeated N_z times to obtain all the N_z values of $\tilde{c}_i(k_x,k_y)$. Once the systems of equations are solved for all (k_x,k_y) , inverse 2D FT is applied to $\tilde{c}_i(k_x,k_y)$, $i=1,...,\ N_z$, to reconstruct a 2D image $c_i(x,y)$ at each $z=z_i$ plane. Then, the normalized modulus of $c_i(x,y)$, $|c_i(x,y)|/L$, where L is the maximum of $|c_i(x,y)|$ for all z_i , is plotted versus x and y to obtain 2D images of the objects at all N_z planes. By putting together all 2D slice images, a 3D image of the object is obtained.

III. Experimental Results

To validate the performance of the proposed imaging technique, we conduct several experiments. Fig. 2 shows the experimental setup. We employ two planar coils manufactured by Texas Instruments [Texas Instruments 2015] called LDC coils H and J connected side-by-side with center-to-center distance of 43 mm. Table 1 shows the parameters for these coils. The use of two different coils with different field strengths allows for distinguishing objects along the depth. These coils are used along with the inductance-to-digital converter data acquisition module (LDC1614) manufactured by Texas

Instruments [Texas Instruments 2016]. LDC1614 board operates based on the inductive sensing technology discussed in the previous section to sense and measure the presence or position of conductive objects. While, in general, the transmitter and receiver coils can be separate (as shown in Fig. 1), here, each coil operates as both transmitter and receiver. Coils H and J, with their self-capacitance, resonate at 1.226 MHz and 2.664 MHz, respectively. As discussed in section II, the changes of resonant frequencies due to the presence of metallic objects are measured by LDC1614 module.

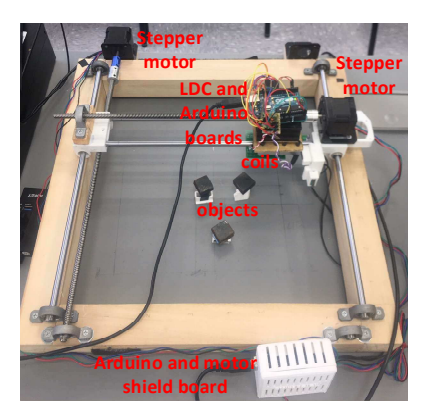


Fig. 2. Experimental setup.

Table 1. Parameters of LDC coils manufactured by Texas Instruments.

| Coil | Shape | Radius (mm) | Layers | Turns/ Layer | Trace Width (mm) | Trace Spacing (mm) |
|------|----------|----------------|--------|-----------------|------------------------|--------------------------|
| Н | circular | 46 | 2 | 50 | 0.15 | 0.15 |
| J | circular | 29 | 2 | 35 | 0.15 | 0.15 |

The coils perform raster scanning of a 2D region with size of 22 cm \times 26 cm. This is implemented via the use of two stepper motors for positioning along the x and y directions. The motors are controlled by PC via an Arduino UNO board and a motor shield board Adafruit V2.3. The number of samples along both x and y directions is 30 samples. The metallic objects employed in the imaging experiments are made of iron with size of 2 cm \times 2 cm \times 0.5 cm. The aim is to reconstruct the images of the objects placed at two planes (at two depths) z=1 cm and z=2 cm, referred to as planes 1 and 2, respectively. The coils are scanned over the z=0 plane.

In the first experiment, we place one object at (x, y) = (16, 7) cm on the first plane and another object at (x, y) = (16, 19) cm on the second plane. Figs. 3(a) and (b) show the raw data measured by the two coils. We apply a threshold that is equal to the 5% of the peak of the measured data to convert the data to a binary image. We then extract the boundary around each peak that could be due to the presence of a metallic object. The boundaries are extracted using Moore-Neighbor tracing algorithm provided in MATLAB [Gonzalez 2004]. These boundaries provide estimations of the locations of the objects which are used as regions of interest (ROIs) for beamspace transformation. We then apply the beamspace approach to each ROI. Figs. 4(a) and (b) show the reconstructed images of the objects over the two planes. It is observed that the two objects are reconstructed successfully on their true positions.

In the second experiment, we place two objects on the first plane at (x, y) = (7, 11) cm and (x, y) = (14, 11) cm and one object on the

Page 4 of 5 IEEE MAGNETICS LETTERS

second plane at (x, y) = (11, 21) cm. The raw data images are shown in Fig. 5. Following the same approach as in the first example, the images shown in Fig. 6 are reconstructed. Again, it is observed that the objects appear in their true positions.

Finally, in the third experiment, we consider one metallic object on the first plane at (x, y) = (11, 9) cm and two metallic objects on the second plane at (x, y) = (9, 21) cm and (x, y) = (16, 21) cm. Figs. 7 and 8 show the raw data and the reconstructed images, respectively. The appearance of the objects in their true positions again confirms the validity of the proposed imaging approach.

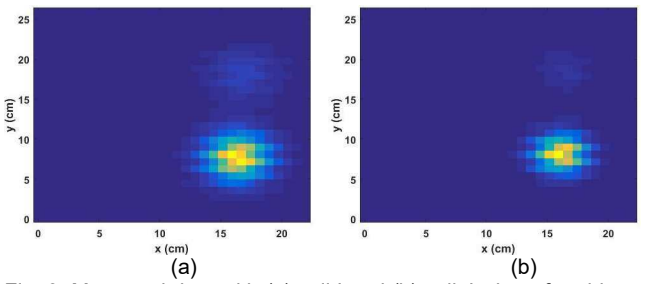


Fig. 3. Measured data with (a) coil I and (b) coil J when, for objects at (x, y, z) = (16, 7, 1) cm and (x, y, z) = (16, 19, 2) cm.

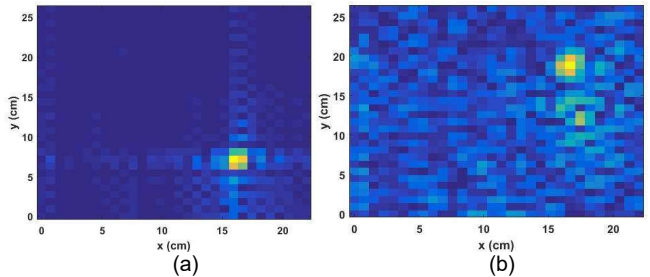


Fig. 4. Reconstructed images at (a) first plane and (b) second plane using the measured data in Fig. 3.

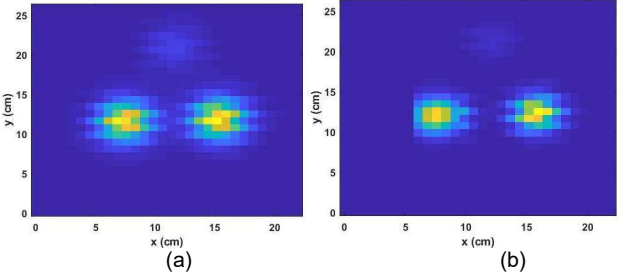


Fig. 5. Measured data with (a) coil I and (b) coil J for objects at (x, y, z) = (7, 11, 1) cm, (x, y, z) = (14, 11, 1) cm, and (x, y, z) = (11, 21, 2) cm.

IV. CONCLUSION

An approach was proposed for reconstructing 2D images of metallic objects at multiple depths. It is based on the inductive sensing technology which is cost-effective and sensitive. The proof-of-concept experiments were conducted using off-the-shelf components.

For a given imaging configuration (specific coils, data acquisition circuitry, imaged medium, and imaged depths), measurements of PSFs are implemented only once and then they are employed for imaging of unknown objects over the corresponding depth using the corresponding setup. In practice, for a given imaging setup, a database of PSFs can be measured *a priori* for various imaged depths. Besides, COs are the smallest possible defects that are measurable at each depth. Thus, their size can be different for different depths and for

different coils. The chosen COs are, in turn, the building blocks for any larger object to be imaged at the corresponding depth.

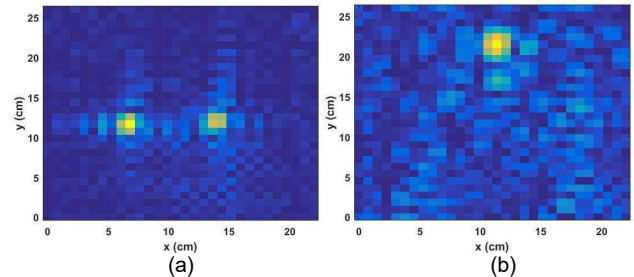


Fig. 6. Reconstructed images at (a) first plane and (b) second plane using the measured data in Fig. 5.

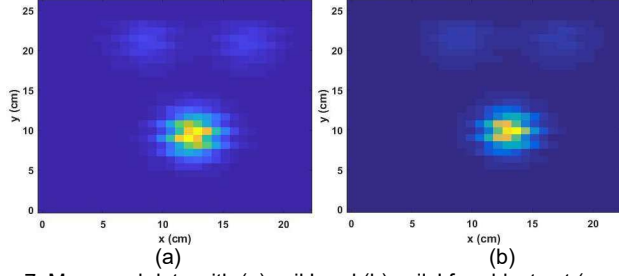


Fig. 7. Measured data with (a) coil I and (b) coil J for objects at (x, y, z) = (11, 9, 1) cm, (x, y, z) = (9, 21, 2) cm, and (x, y, z) = (16, 21, 2) cm.

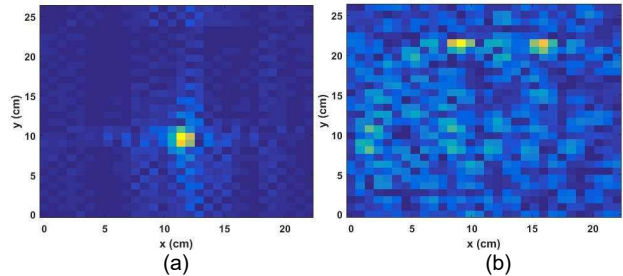


Fig. 8. Reconstructed images at (a) first plane and (b) second plane using the measured data in Fig. 7.

Higher depth sensitivity and better depth resolution can be achieved using larger coils and larger difference between the coils (in size, number of turns, number of layers, or core materials), respectively.

As a near-field electromagnetic imaging system, the lateral resolution depends on the dimensions of the coils and the noise floor of the data acquisition system, e.g., see [Tabib-Azar 1999]. Maximum depth range depends on the field strength of the coils, and the shape, size, and composition of the metallic object. For the utilized coils, according to the manufacturer, the depth sensitivity is almost in the order of coil's diameter [Texas Instruments 2018]. Furthermore, the spatial sampling rate of the responses can be determined based on the Nyquist sampling criteria. For instance, if the spatial spectrum of the collected PSF along x axis has maximum bandwidth of k_x^m , the minimum spatial sampling rate becomes $2k_x^m$.

The processing which is based on convolution theory and beamspace transformation is fast and robust and can be implemented within few seconds on a regular computer. Thus, quasi real-time imaging can be realized, in future, using an array of sensors (instead of mechanical scanning implemented in this work) to expedite the data acquisition process.

IEEE MAGNETICS LETTERS Page 5 of 5

ACKNOWLEDGMENT

This project has been partially supported by Research Experiences for Undergraduates (REU) Site award provided by US National Science Foundation (NSF), award No. 1852316.

REFERENCES

- Darrer B J, Watson J C, Bartlett P, Renzoni F (2015) "Electromagnetic imaging through thick metallic enclosures," AIP Advances 5, vol. 087143, pp. 1-8.
- Darrer B J, Watson J C, Bartlett P, Renzoni F (2015) "Magnetic imaging: a new tool for UK national nuclear security," *Scientific Reports*, vol. 5, no. 7944.
- Du L, Zhe J (2012) "Parallel sensing of metallic wear debris in lubricants using undersampling data processing," *Tribology International*, vol. 53, pp. 28-34.
- Du L, Zhu X, Han Y, Zhao L, Zhe J (2013) "Improving sensitivity of an inductive pulse sensor for detection of metal wear debris in lubricants using parallel LC resonance method," Meas. Sci. Technol., vol. 24, no. 7, pp. 1-10.
- Higson S R, Drake P, Stamp D W, Peyton A, Binns R, Lyons A, Lionheart W (2003) "Development of a sensor for visualization of steel flow in the continuous casting nozzle," *Revue de Metallurgie-Cahiers d'Informations Techniques 100*, pp. 629-632.
- Gaydecki P, Quek S, Miller G, Fernandes B T, Zaid M A M (2002) "Design and evaluation of an inductive Q-detection sensor incorporating digital signal processing for imaging of steel reinforcing bars in concrete," *Meas. Sci. Technol.*, vol. 13, pp. 1327-1335.
- Gogola D, Krafčík A, Štrbák O, Frollo I (2013) "Magnetic resonance imaging of surgical implants made from weak magnetic materials," *Measurement Science Review*, vol. 13, no. 4
- Griffiths H (2001) "Magnetic induction tomography: a measuring system for biological tissues," *Meas. Sci. Technol.*, vol. 12, pp. 1126-1131.
- Gonzalez R C, Woods R E, Eddins S L (2004) Digital Image Processing Using MATLAB, New Jersey, Pearson Prentice Hall.
- Guilizzoni R, Watson J C, Bartlett P, Renzoni F (2015) "Imaging by electromagnetic induction with resonant circuits," Proc. SPIE, Image Sensing Technologies: Materials, Devices, Systems, and Applications II, vol. 94810Q (2015).
- Guilizzoni R, Watsonb J C, Bartletta P A, Renzonia F (2016) "Electromagnetic Induction Imaging of concealed metallic objects by means of resonating circuits." Proc. SPIE.

- Detection and Sensing of Mines, Explosive Objects, and Obscured Targets XXI, vol. 98230P-1.
- Ledger P D, Lionheart W R B (2015) "Characterizing the shape and material properties of hidden targets from magnetic induction data," *IMA Journal of Applied Mathematics*, vol. 80, no. 6, pp. 1776-1798.
- Ma L, Wei H-Y, Soleimani M (2013) "Planar magnetic induction tomography for 3D near subsurface imaging," *Prog. Electromagn. Res.*, vol. 138, pp. 65-82.
- Oppenheim A V, Schafer R W, Buck J R (1999) Discrete-Time Signal Processing, 2nd ed.; Prentice Hall: Upper Saddle River, NJ, USA, 1999.
- Peyton A J, Yu Z Z, Lyon G, Al-Zeibak S, Ferreira J, Velez J, Linhares F, Borges A R, Xiong H L, Saunders N H, Beck M S (1996) "An overview of electromagnetic inductance tomography: description of three different systems," *Meas. Sci. Technol.*, vol. 7, pp. 261-271.
- Rodriguez-Rivera A, V.Baryshnikov B, VanVeen B D, Wakai R T (2006) "MEG and EEG source localization in beamspace," *IEEE Trans. Biomed. Eng.*, vol. 53, no. 3, pp. 430-441.
- Szymanik B, Frankowski P K, Chady T, Chelliah C R A J (2016) "Detection and inspection of steel bars in reinforced concrete structures using active infrared thermography with microwave excitation and eddy current sensors," Sensors, vol. 16 (2), no. 234.
- Tabib-Azar M, Katz J L, LeClair S R (1999) "Evanescent microwaves: a novel superresolution noncontact nondestructive imaging technique for biological applications," *IEEE Trans. Inst. Meas.*, vol. 48, no. 6, pp. 1111-1116.
- Texas Instruments, LDC Reference Coils User's Guide, Literature Number: SNOU136, May 2015, http://www.ti.com/lit/ug/snou136/snou136.pdf
- Texas Instruments, LDC131x and LDC161x EVM User's Guide, Literature Number: SNOU135A, Revised September 2016, http://www.ti.com/lit/ug/snou135a/snou135a.pdf
- Texas Instruments, LDC1312, LDC1314 Multi-Channel 12-Bit Inductance to Digital Converter (LDC) for Inductive Sensing, 2018, http://www.ti.com/lit/ds/symlink/ldc1312.pdf
- Wei H Y, Soleimani M (2012) "A magnetic induction tomography system for prospective industrial processing applications," *Chinese J. Chem. Eng.*, vol. 20, no. 2, pp. 406-410
- Zolgharni M, Griffiths H, Ledger P D (2010) "Frequency-difference MIT imaging of cerebral haemorrhage with a hemispherical coil array: numerical modelling," *Physiol. Meas.*, vol. 31, pp. S111-S125.